PHYSICAL REVIEW B VOLUME 49, NUMBER 11 15 MARCH 1994-I

Spatiotemporal behavior of localized current filaments in *p-n-p-n* diodes: Numerical calculations and comparison with experimental results

F.-J. Niedernostheide, M. Ardes, M. Or-Guil, and H.-G. Purwins
Institut für Angewandte Physik, Universität Münster, Corrensstraße 2/4, D-48149 Münster, Germany

(Received 9 September 1993)

A two-component evolution equation of reaction-diffusion type derived recently to describe experimental results on the self-organization of current-density filaments in silicon *p-n-p-n* diodes has been solved numerically. By using physically reasonable parameters and applying different boundary conditions, good qualitative agreement with experimental results is obtained. In particular, the following bifurcation scenario obtained by increasing the external driving voltage in the experiment can be reproduced in the calculations: stationary homogeneous current-density distribution leads to static current filament leads to rocking current filament leads to traveling current filament. Furthermore, it is shown that a period-doubling cascade of integral system variables, as, e.g., the device voltage, strongly correlates with the spatiotemporal filament motion which undergoes the same period-doubling route. Even quantitative agreement between numerical and experimental results could be achieved to some extent.

I. INTRODUCTION

Self-organized spatiotemporal structures can appear in semiconductors in the form of current-density filaments or electric-field domains and are usually connected with the appearance of negative differential conductivity resulting in an S-shaped or N-shaped current-voltage characteristic, respectively. In experiments, current-density filaments have been observed in bulk materials, e.g., *n*-type GaAs,[1-4] and *p*-type Ge,[5] as well as in semiconductor devices, e.g., SiC *p-n* junctions,[6] Si *p-i-n* diodes,[7] and *p-n-p-n* diodes.[8-10] Specific models describing the formation of static current-density filaments and the dynamical behavior of filaments have only been developed in a few cases. Examples are *p-n* junctions,[6,11] heterostructure diodes,[12] *p-n-p-n* diodes,[8] or bulk semiconductors in the low-temperature regime.[13,14]

In this paper, we start from the two-layer model for spatial and spatiotemporal pattern formation in special p^+-n^+-p-n^- diodes derived in Ref. 8. A short review of the main features of the model and the appertaining model equations is given in Sec. II. In Sec. III we present results of numerical calculations of the model equations, which describe essentially the evolution of the current density and the potential in the interface layer. In agreement with the predictions made on the basis of qualitative analytical arguments,[8] it is shown that the calculations yield all bifurcations observed experimentally. The influence of different boundary conditions on the evolution and the dynamics of the observed current filaments is studied in order to get insight into the interaction mechanism between the boundary of the system and the filament. In Sec. IV the numerical results are compared in detail with experimental results, and, finally, some conclusions are drawn.

II. THE MODEL

For a detailed derivation of the model equations we refer the reader to Ref. 8; here we restrict ourselves to summing up the main features of the model and writing down the final equations. The basic idea for modeling the spatial and spatiotemporal behavior of current-density filaments in p^+-n^+-p-n^- diodes is founded on the division of the device into two parts, a p^+-n^+-p transistor and a p-n^- junction as shown in Fig. 1. The p^+-n^+-p transistor works as an avalanche transistor: if the electric field in the reverse-biased n^+-p junction reaches a critical value impact ionization takes place. The generated electron-hole pairs are separated by the electric field and the electrons reaching the p^+-n^+ emitter cause an additional injection of holes into the n^+ base. This combination of an autocatalytic mechanism due to the avalanche process in the n^+-p collector and the positive feedback mechanism based on the additional hole injection leads to the S-shaped current-voltage characteristic of the p^+-n^+-p transistor.

The device is considered to be quasi-two-dimensional, i.e., the current-density and the potential distributions do not vary in the *z* direction (Fig. 1). For the description of the p^+-n^+-p transistor the following assumptions have been made.

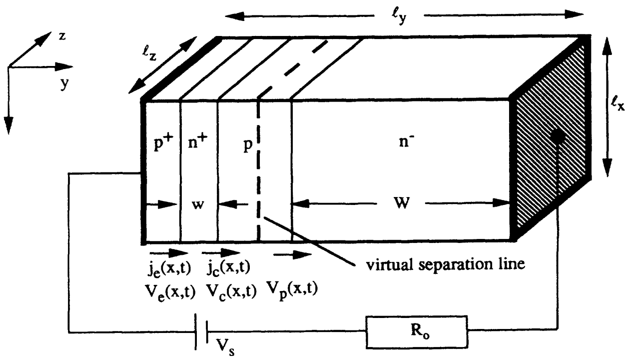

FIG. 1. Schematic outline of the p^+-n^+-p-n^- device and the electrical circuit; typical dimensions are $l_x = 1$–5 mm, $l_y = 400$–800 μm, $l_z = 400$–1000 μm.

0163-1829/94/49(11)/7370(15)/$06.00 49

(i) The current density $j_e(x,t)$ of the p^+-n^+ emitter is the sum of the displacement current density $C_e \partial V_e/\partial t$, the current density $j_s[\exp\{V_e(x,t)/V_T\}-1]$ arising from the diffusion of injected holes into the n^+ base, and the recombination current density $j_r[\exp\{V_e(x,t)/2V_T\}-1]$:

$$j_e(x,t)=C_e\frac{\partial V_e}{\partial t}+j_s\left[\exp\left[\frac{V_e}{V_T}\right]-1\right]+j_r\left[\exp\left[\frac{V_e}{2V_T}\right]-1\right] .$$

(ii) The current density $j_c(x,t)$ of the n^+-p collector is the sum of the collector saturation current density j_{SC}, the transfer current density of holes $\beta j_s[\exp\{V_e(x,t)/V_T\}-1]$ injected from the p^+-n^+ emitter, both being multiplied by the multiplication factor $M(V_c)=[1-(V_c/V_b)^m]^{-1}$ due to the avalanche effect, and the leakage current density $V_c(x,t)/\rho_L$:

$$j_c(x,t)=Mj_{\mathrm{SC}}+M\beta j_s\left[\exp\left[\frac{V_e}{V_T}\right]-1\right]+\frac{V_c}{\rho_L} .$$

(iii) In order to take into account the spreading of the current in the n^+ base, we connect the emitter and collector current densities by the following equation:

$$j_e(x,t)=j_c(x,t)+w\sigma_b\partial^2V_e(x,t)/\partial x^2 .$$

For a listing of the parameters see Table I.

Using these assumptions the evolution of the emitter voltage V_e is determined by

$$C_e\frac{\partial V_e(x,t)}{\partial t}=w\sigma_b\frac{\partial^2 V_e(x,t)}{\partial x^2}-q(V_e,V_i) , \tag{1}$$

with $q(V_e,V_i)$ defined as

$$q(V_e,V_i)=[1-\beta M]j_s\left[\exp\left[\frac{V_e}{V_T}\right]-1\right]+j_r\left[\exp\left[\frac{V_e}{2V_T}\right]-1\right]-Mj_{\mathrm{SC}}-\frac{V_i-V_e}{\rho_L} . \tag{2}$$

$V_i(x,t)=V_e(x,t)+V_c(x,t)$ is the voltage drop across the entire p^+-n^+-p transistor and, therefore, M can be written also as $M=M(V_i-V_e)$.

The p-n^- junction is considered as an ideal Shockley diode. As outlined in detail in Ref. 8, the evolution of the average hole density $\bar{p}(V_i(x,t))$ in the n^- region obtained by integrating the continuity equation for the hole concentration $p(x,y,t)$ over the y axis (Fig. 1), is given by

$$\tau\frac{\partial\bar{p}(V_i)}{\partial t}=L^2\frac{\partial^2\bar{p}(V_i)}{\partial x^2}+Q(V_e,V_i,V) , \tag{3}$$

where $Q(V_e,V_i,V)$ has the form

$$Q(V_e,V_i,V)=\frac{\tau}{eW}\left\{Mj_{\mathrm{SC}}+\beta Mj_S\left[\exp\left[\frac{V_e}{V_T}\right]-1\right]+\frac{V_i-V_e}{\rho_L}\right\}-\{\bar{p}(V_i,V)-p_{n0}\} , \tag{4}$$

and $\bar{p}(V_i(x,t))$ depends exponentially on V_i:

$$\bar{p}(V_i,V)=p_{n0}\exp\left[\frac{V_p}{V_T}\right]=p_{n0}\exp\left[\frac{V-V_i}{V_T}\right] . \tag{5}$$

$\tau=(\tau_p^{-1}+\tau_s^{-1})^{-1}$ is an effective lifetime determined by the lifetime τ_p of holes in the n^- region and the surface recombination rate τ_s^{-1} at the cathode. V is the voltage drop across the entire p^+-n^+-p-n^- diode. $V_p(x,t)=V-V_i(x,t)$ denotes the voltage drop across the p-n^- junction. For a complete listing of the parameters see again Table 1.

Equations (1) and (3) form a set of evolution equations for the emitter voltage V_e and the transistor voltage V_i, which is determined by the hole density via Eq. (5). If the device is driven by a constant dc driving voltage source V_s, V_e and V_i can be calculated by these equations with $V=V_s$. In experiment, the device is usually operated via a load resistor R_0. Then we have to take into account a third equation resulting from the external circuit:

$$V=V_s-R_0l_z\int_0^{l_x}j(x,t)dx , \tag{6}$$

where $j(x,t)$ is the current density in the device chosen at an arbitrary cross section parallel to the metallic contacts. l_x and l_z denote the width of the sample in the corresponding direction. For numerical calculations we choose the collector current density:

$$j=j_c(V_e,V_i)=Mj_{\mathrm{SC}}+\beta Mj_s\left[\exp\left[\frac{V_e}{V_T}\right]-1\right]+\frac{V_i-V_e}{\rho_L} . \tag{7}$$

The set of Eqs. (1), (3), and (6) has to be completed by specifying suitable boundary conditions of the space-dependent variables V_e and $\bar{p}$. We have studied the following two cases.

Case A. Homogeneous Neumann boundary conditions for V_e and $\bar{p}$:

$$\frac{\partial V_e(x=0,t)}{\partial x}=0 , \quad \frac{\partial V_e(x=l_x,t)}{\partial x}=0 , \tag{8a}$$

$$\frac{\partial\bar{p}(x=0,t)}{\partial x}=0 , \quad \frac{\partial\bar{p}(x=l_x,t)}{\partial x}=0 . \tag{8b}$$

Equation (8a) means that there is no lateral current in the n^+ base at the sample boundaries and Eq. (8b) is physically reasonable to ensure that no lateral diffusion at the sample boundaries takes place in the n^- region.

Case B. Mixed boundary conditions, i.e., Dirichlet boundary conditions for V_e and homogeneous Neumann boundary conditions for $\bar{p}$:

$$V_e(x=0,t)=V_{e0}\ , \quad V_e(x=l_x,t)=V_{e0}\ , \tag{9a}$$

$$\frac{\partial \bar{p}(x=0,t)}{\partial x}=0\ , \quad \frac{\partial \bar{p}(x=l_x,t)}{\partial x}=0\ . \tag{9b}$$

The Dirichlet condition for V_e may be useful if the emitter voltage is limited or fixed, e.g., by surface recombination.

The evolution of the two system variables V_e and $\bar{p}$ is based on a competition process between the variables. This can be seen easily when we consider the device under such a large bias voltage that avalanche multiplication in the n^+-p junction takes place. The generated electrons move to the p^+-n^+ emitter and cause there an additional injection of holes leading to an autocatalytic increase of V_e. j_e then increases, too, because it depends exponentially on V_e. Because of the activating property of V_e in this range we call V_e, and loosely j_e or j_c, too, an activator. An increase of V_e connected with a growth of j_e and j_c leads to an increase of the holes injected in the

Parameter	Parameter meaning and manner of determination	Standard parameter value (typical parameter range)
C_e	capacity per unit square of the p^+-n^+ junction; estimated by the doping profile, see Ref. 9	1×10^{-4} F/cm^2 10^{-2}–10^{-6} F/cm^2
D_p	diffusion coefficient of holes in the n^- layer; determined from literature, see, e.g., Ref. 25	10 cm^2/s 5–20 cm^2/s
j_r	saturation current density of the recombination current in the p^+-n^+ junction; determined by fitting the experimental to the numerical $I(V)$ characteristic	3×10^{-7} A/cm^2 10^{-5}–10^{-8} A/cm^2
j_s	saturation current density of the diffusion current in the p^+-n^+ junction; determined by fitting the experimental to the numerical $I(V)$ characteristic	1.5×10^{-11} A/cm^2 10^{-11}–10^{-14} A/cm^2
j_{SC}	saturation current density of the n^+-p collector; determined by fitting the experimental to the numerical $I(V)$ characteristic	2×10^{-8} A/cm^2 10^{-8}–10^{-14} A/cm^2
l_x	sample width in x direction; measured after finishing preparation procedure	0.5 cm 0.1–1.0 cm
l_z	sample width in z direction; measured after finishing preparation procedure	0.05 cm 0.03–0.1 cm
L	effective diffusion length of holes in the n^- region; defined by $L=(D_p\tau)^{1/2}$	0.02 cm 0.01–0.05 cm
m	coefficient determining the dependence of the multiplication factor on the collector voltage; determined from literature, e.g., Ref. 25	3 2–5
p_{n0}	equilibrium concentration of holes in the n^- layer; determined by the doping profile, see Ref. 9	1×10^{7} cm^{-3} 10^{7}–3×10^{7} cm^{-3}
R_0	external load resistor	1 Ω 0.1–10^6 Ω
T	temperature	300 K 77–370 K
V_b	breakdown voltage of the n^+-p collector; determined by fitting the experimental to the numerical $I(V)$ characteristic	42 V 35–45 V
V_T	thermal voltage; defined by kT/e, with Boltzmann constant k and elementary charge e	0.026 V 0.0065–0.032 V
w	thickness of the n^+ base; determined by the doping profile, see Ref. 9; the influence of a drift field in the base may be taken into account by an effective base width smaller than the real one	0.0003 cm 10^{-4}–10^{-3} cm
W	thickness of the n^- substrate; determined by the doping profile, see Ref. 9	0.06 cm 0.04–0.08 cm
β	base transport factor; determined by fitting the experimental to the numerical $I(V)$ characteristic	0.6 0.5–0.9
ρ_L	leakage resistance of the collector; determined by fitting the experimental to the numerical $I(V)$ characteristic	40 000 Ω cm^2 10^4–10^5 Ω cm^2
σ_b	average conductivity of the n^+ base; determined by the doping profile, see Ref. 9	10 (Ω cm)$^{-1}$ 1–100 (Ω cm)$^{-1}$
τ	effective hole lifetime; defined by the hole lifetime in the n^- region and the surface recombination rate at the cathode	10 μs 10–300 μs

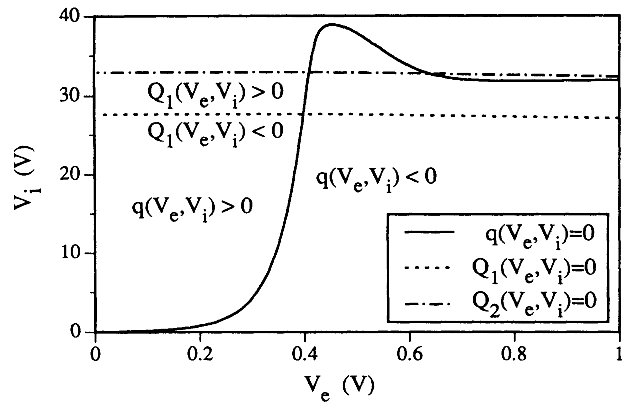

FIG. 2. Null-cline system of Eqs. (1) and (3) for parameters of Table I, but $R_0 = 0\ \Omega$; V_s has been chosen as 28.0 and 33.2 V for Q_1 and Q_2, respectively.

n^- layer and consequently to an increase of V_p according to Eq. (5). This results in a decrease of $V_i = V - V_p$, the latter being valid if the device voltage is kept constant. Thus, the inhibiting process based on the properties of the p-n^- junction counteracts the autocatalytic process in the p^+-n^+-p transistor. The voltage V_i or V_p may therefore be called the inhibitor. Furthermore, the load resistor effects a global inhibition that may have an important influence on the creation of spatiotemporal patterns.[8,15–17]

In order to get an insight into the possible behavior of the system it is helpful to look at the null-cline system of Eqs. (1) and (3) for homogeneous distributions of V_e and $\bar{p}$; i.e., we have to find the solutions of the equations $q(V_e, V_i) = 0$ and $Q(V_e, V_i(\bar{p}); V) = 0$. In Fig. 2 the curves $V_i\ (V_e)$ are drawn as they result for a parameter set under voltage-bias conditions, i.e., without a load resistor. The curves $Q_1 = 0$ and $Q_2 = 0$ have a small negative slope and belong to different values of the voltage source V_s with $V_{s2} > V_{s1}$. A variation of V_s leads to a vertical shift of the curve $Q = 0$. Depending on V_s it is therefore possible to realize one, two, or three intersection points of the curves $q = 0$ and $Q = 0$. Since the intersection points of the null clines correspond to homogeneous stationary solutions of the system, it is clear that the system can realize for a given set of parameters up to three stationary pairs (V_e, V_i) of the emitter and collector voltage. However, not all these states are stable, and inhomogeneous distributions and/or nonstationary distributions can be expected.

III. NUMERICAL RESULTS

The numerical calculations have been performed on a parallel computer consisting of nine transputers of type T800. As discretization technique the finite-difference method has been used; in particular the Crank-Nicolson method has been applied for discretization in time. For the solution of the implicit equations corresponding to Eqs. (1) and (3), we have used a relaxation method that is a simplified version of the Newton-single-step method. The third equation, Eq. (6), involving the integral term, has been solved by introducing a time dependence of the device voltage V with an effective relaxation-time constant which is at least two orders of magnitude faster than that of the other system variables V_e and V_i.

In what follows, we present results of numerical calculations with different boundary conditions performed with reference to experiments. In particular, the spatial and temporal evolution of the activating and the inhibiting variables are analyzed in terms of their dependence on the value of the dc driving voltage V_s. The parameters for the numerical calculations have been estimated partly from experiments and partly from the literature, as summarized in Table I.

A. Calculations using homogeneous Neumann boundary conditions

1. Transition from a homogeneous current-density distribution to a static localized filament

As initial values, we choose spatially homogeneous distributions for V_e and $\bar{p}$. In order to simulate statistical fluctuations, which are unavoidable in real systems, a pseudorandom variable of about 0.01% of the corresponding values is added to both distributions in each time step. For a given value of V_s and the initial distributions, new steady-state distributions of V_e and $\bar{p}$ are calculated via Eqs. (1), (3), and (6) and are used as initial conditions for the next value of V_s. In Fig. 3(a), the calculated total current-voltage characteristic $I(V)$ of the device obtained by increasing V_s is depicted. For low values of the device voltage V, only a very small total current distributed homogeneously is allowed to flow through the p^+-n^+-p-n^- diode. The current limitation is governed by the reverse-biased n^+-p junction. If the voltage drop V_c across this junction approaches the value of $V_b \approx 40$ V, the multiplication factor $M(V_c)$ increases significantly. The maximum value of M at breakdown is about 5. The steady-state distributions of the voltages V_e and V_i are homogeneous for the blocking branch and, therefore, those of the current densities j_e and j_c are too. Even in the region with negative differential resistance, where steady states are obtained if the load resistor in the external circuit is sufficiently large (typically $R_0 \geq 10$ kΩ), the calculated distributions are homogeneous up to a total device current of $I \approx 0.4$ mA, indicated as point A on the $I(V)$ characteristic in Fig. 3(a). The corresponding homogeneous distributions of j_c and V_p for this current are shown in the uppermost diagram of Fig. 3(b). Here and in what follows, we have drawn the current density $j_c(V_e, V_i)$ and the potential $V_p = V - V_i(\bar{p})$ instead of V_e and $\bar{p}$ because these variables can most easily be compared with experimental results (cf. Sec. IV). In doing so, one has in mind that j_c essentially represents the activator whereas V_p corresponds to the inhibitor. At the point B, where the negative differential resistance reaches approximately its minimum value, the current-density distribution starts to contract, whereas the potential distribution V_p remains nearly homogeneous. However, if we proceed along the $I(V)$ characteristic to larger current values, V_p becomes inhomogeneous, too [point C,

Fig. 3(b)]. Both the current-density distribution and the potential contract further with increasing total current (D) until they reach a minimum width (E). This contraction phase is strongly connected with the pronounced negative-differential-resistance region in the $I(V)$ characteristic, where the inequality $\beta M \gg 1$ holds. Note that all distributions drawn in Fig. 3(b) are stable stationary solutions of the set of Eqs. (1), (3), and (6) and the process of contraction is completely reversible at any stage. When the contraction phase is completed a stable localized current-density filament has been formed. Thereby a filament is considered to be localized if the values of the system variables V_e and $\bar{p}$, and consequently the values of j_e, j_c, and V_i, far away from the center of the filament, are solutions of the homogeneous steady-state problem: $q=0$ and $Q=0$.

For an analysis of the contraction from the homogeneous current density distribution to a localized filament, we consider the dependence of its width, more precisely the full width Δ at half maximum, on the total current I. Filaments as shown in Fig. 3 are considered as half filaments. The result of an evaluation of the calculated steady-state distributions of $j_c(x)$ and $V_p(x)$ is shown in Fig. 4, where Δj_c and ΔV_p are drawn as functions of the total current I. The contraction phase takes place in the current interval $I \in [0.4, 20 \text{ mA}]$. The minimum values of the widths Δj_c and ΔV_p are 0.33 and 1.7 mm, respectively. The quite broad distribution of V_p with respect to j_c is analogous to solutions of conventional reaction-diffusion systems of activator-inhibitor type, in which localized structures can be stabilized by a fast inhibitor with rather large diffusion length in comparison with a slowly acting activator characterized by a relative short diffusion length.[18]

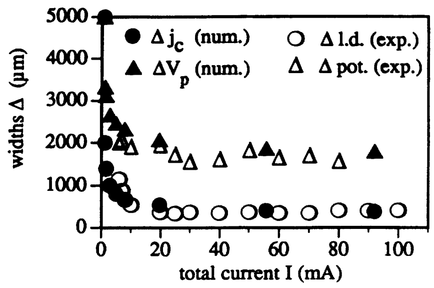

FIG. 4. Full widths Δj_c and ΔV_p at half maximum obtained from the calculated steady-state distributions j_c and V_p as functions of the total current I; parameters as in Table I but $R_0 = 10$ kΩ; the open symbols represent results from experiments and mark the full widths Δ at half maximum of the light density (l.d.) and potential distribution (pot.) in a p-n-p-n diode as functions of the current I (cf. Sec. IV).

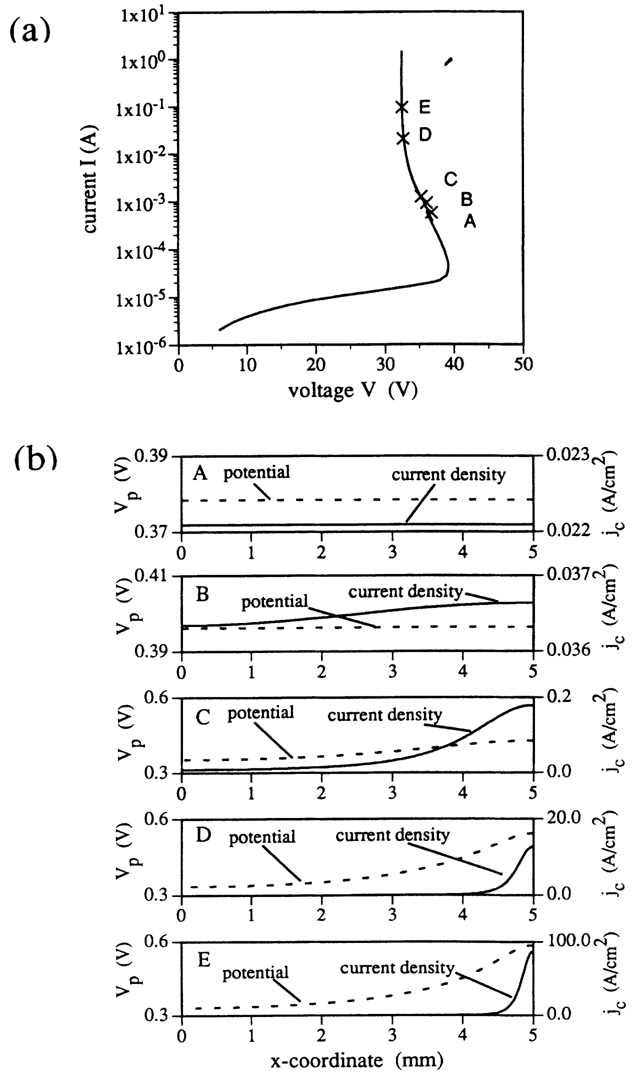

FIG. 3. (a) Numerically calculated current-voltage characteristic $I(V)$ and (b) stationary spatial distributions of V_p and j_c for different values of the driving voltage V_s indicated as points A–E; (V_s, I)=(40.826 V,0.56 mA) (A), (45.2 V,0.9 mA) (B), (47.61 V,1.2 mA) (C), (229.4 V,19.7 mA) (D), (952.4 V, 92 mA) (E); other parameters as in Table I but $R_0 = 10$ kΩ.

It is conspicuous that the localized structures shown in Fig. 3 always develop near one of the system boundaries. The boundary at which the filament rises is selected by random fluctuations of the system variables included in the numerical calculation. If we choose a filament in the center of the system as initial condition, this filament moves to one of the boundaries and becomes stable again as a half filament. The velocity of this moving process is governed by the ratio of the relaxation-time constants of the activating and the inhibiting component V_e and V_i, respectively, and can be slowed down essentially by, e.g., increasing the emitter capacity C_e. For sufficiently large C_e, say an increase of C_e from 10^{-4} to 10^{-2} F/cm^2, the filament can be stabilized at any arbitrary point.

2. Transition from a static to a breathing localized filament

The static filament is stable only up to a certain critical total current I_{c1} corresponding to a critical width of the filament. When this critical value is reached the wall of the filament becomes unstable and a breathing filament develops, i.e., the filament width widens and narrows periodically. In Fig. 5 the time evolution of the current density j_c is shown for different values of the applied dc driving voltage V_s. The dark areas mark those parts of

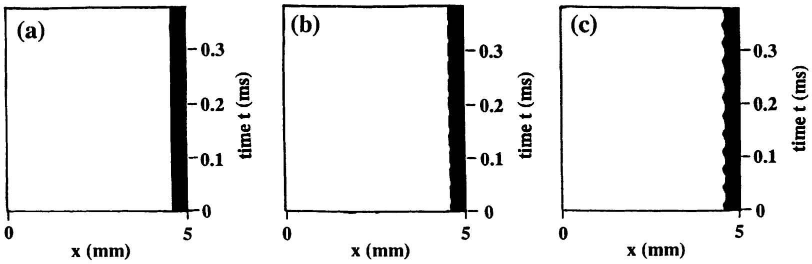

FIG. 5. Numerically calculated spatiotemporal evolution of $j_c(x,t)$ for different values of V_s; parameters as in Table I and $(V_s,\bar{I})=(33.890\ \mathrm{V},1.445\ \mathrm{A})$ (a), (33.895 V,1.450 A) (b), (33.900 V,1.455 mA) (c).

the distribution in which a certain threshold value, approximately $\frac{2}{3}$ of the maximum current density, is exceeded. Thus, these regions correspond to high-current regions and indicate the spatial position of the current filament. For $V_s=33.890$ V [Fig. 5(a)] the distribution is still stable, whereas for $V_s=33.895$ V [Fig. 5(b)] a small modulation of one of the filament walls becomes visible; the amplitude of this wall oscillation increases continuously with increasing V_s as shown in Fig. 5(c), where $V_s=33.900$ V has been chosen. The wall oscillations are accompanied by oscillations of the total current $I(t)$ and of the voltage drop $V(t)$ across the device. The period of these oscillations is the same as the period of the wall oscillations.

A detailed analysis of the spatial motion is possible if we investigate the spatial distributions of $j_c(x,t)$ and $V_p(x,t)$ at different stages of the oscillation period, as shown in Fig. 6. In Fig. 6(a), the points of time t_i, $i=1$–6, chosen to represent $j_c(x,t_i)$ and $V_p(x,t_i)$ are related to the time trace $V(t)$ of the voltage drop across the device. As can be seen from the spatial distributions in Fig. 6(b), there is a modulation of the amplitude of the current density in addition to the breathing oscillation. The amplitude oscillation is about 30% of the maximum value of j_c. The interplay between the amplitude and the breathing oscillation is such that the total current oscillates with a quite small amplitude, typically in the range of a few tenths of a percent to a few percent of the dc current part, depending on the value of R_0. The maximum elongation of the wall in the direction of large x values corresponds to a maximum total current $I(t)$, carried essentially by the filament, and a minimum in $V(t)=V_s-R_0I(t)$. A comparison of the distributions $V_p(x,t)$ with the corresponding current-density distributions $j_c(x,t)$ at t_1 and t_3, which correspond to a maximum and minimum of the wall elongation of j_c, reveals that there is a time delay between the movement of both distributions. The potential distribution representing the inhibitor follows behind the current-density distribution, which represents the activator, as a result of the larger relaxation-time constant determined by the effective lifetime τ of holes in the n^- layer. We remark that the variations of V_p are quite small and, therefore, they cannot be resolved in Fig. 6(b).

For different values of R_0 (values from 0.1 Ω to 10 kΩ have been used together with the parameter set of Table I), the transition from a static to a breathing current filament occurs in all cases at the same critical current value $I_{c1}=1.447$ A. Therefore, the total current seems to be the proper bifurcation parameter rather than the value of V_s, the critical value of which changes if R_0 is changed. In order to characterize the bifurcation type from the static to the oscillating filament it is therefore reasonable to consider the amplitude V_0 of the ac part of the device voltage $V(t)$ and the amplitude l_p of the wall oscillations of j_c, defined by half the distance of the maximum and minimum wall elongation, as functions of the arithmetic mean $\bar{I}$ of the total current I. As a result, we obtain that both quantities V_0 and l_p increase in a square-root-like

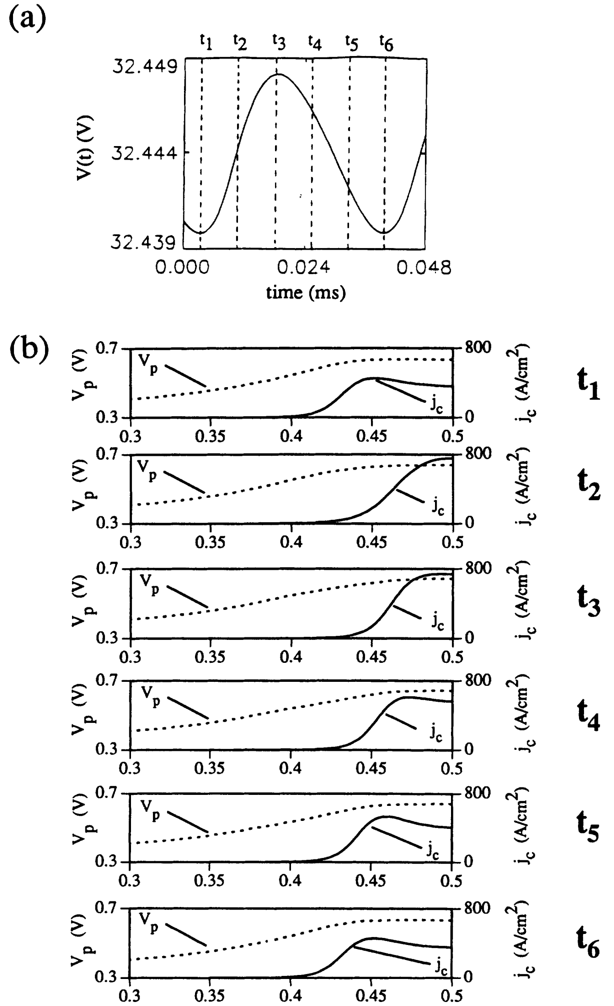

FIG. 6. Numerically calculated time trace $V(t)$ of the device voltage (a) and distributions $V_p(x)$ and $j_c(x)$ for different times during an oscillation period (b); parameters as in Table I and $V_s=33.94$ V, $\bar{I}=1.4896$ A, $t_1=2$ μs, $t_2=9.5$ μs, $t_3=17$ μs, $t_4=24.5$ μs, $t_5=32$ μs, $t_6=39.5$ μs with respect to the time zero in (a).

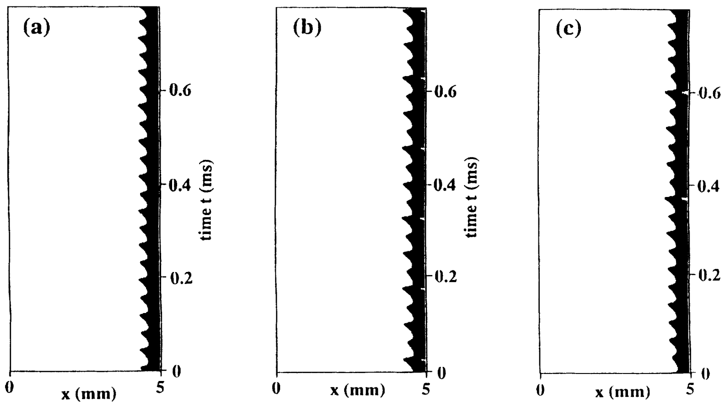

FIG 7. Numerically calculated spatiotemporal evolution of $j_c(x,t)$ for different values of V_s; parameters as in Table I and $(V_s,\bar{I})=(33.9450\ \mathrm{V}, 1.501\ \mathrm{A})$ (a), (33.9495 V,1.510 A) (b), (33.9505 V,1.511 A) (c).

manner with $\bar{I}$. In contrast to this continuous growing of V_0 and l_p starting from zero at $\bar{I}=I_{c1}$, the oscillation at the bifurcation point sets in with a value of the fundamental frequency definitely larger than zero. This value decreases when $\bar{I}$ is increased. Thus, the transition shows typical features of the well-known supercritical Hopf bifurcation.

3. Period-doubling cascade of an oscillating localized filament

The simple periodic filament motion is stable in a current interval from $\bar{I}=1.447-1.500$ A. For larger average currents, the spatiotemporal motion undergoes a period-doubling cascade. The threshold diagrams in Figs. 7(a)–7(c) show a period-2 motion, a period-4 motion, and a motion which reveals no periodicity during the total recording time (12 ms) for values of $V_s=33.9450$, 33.9495, and 33.9505 V corresponding to an average current of $\bar{I}=1.501$, 1.510, and 1.511 A, respectively. The time traces $V(t)$ belonging to the diagrams of Fig. 7 are shown in Fig. 8. Evidently, the period-2 and period-4 oscillations of the filament wall are accompanied by respective oscillations of the voltage signal $V(t)$. Accordingly, the time trace $V(t)$ of the non-

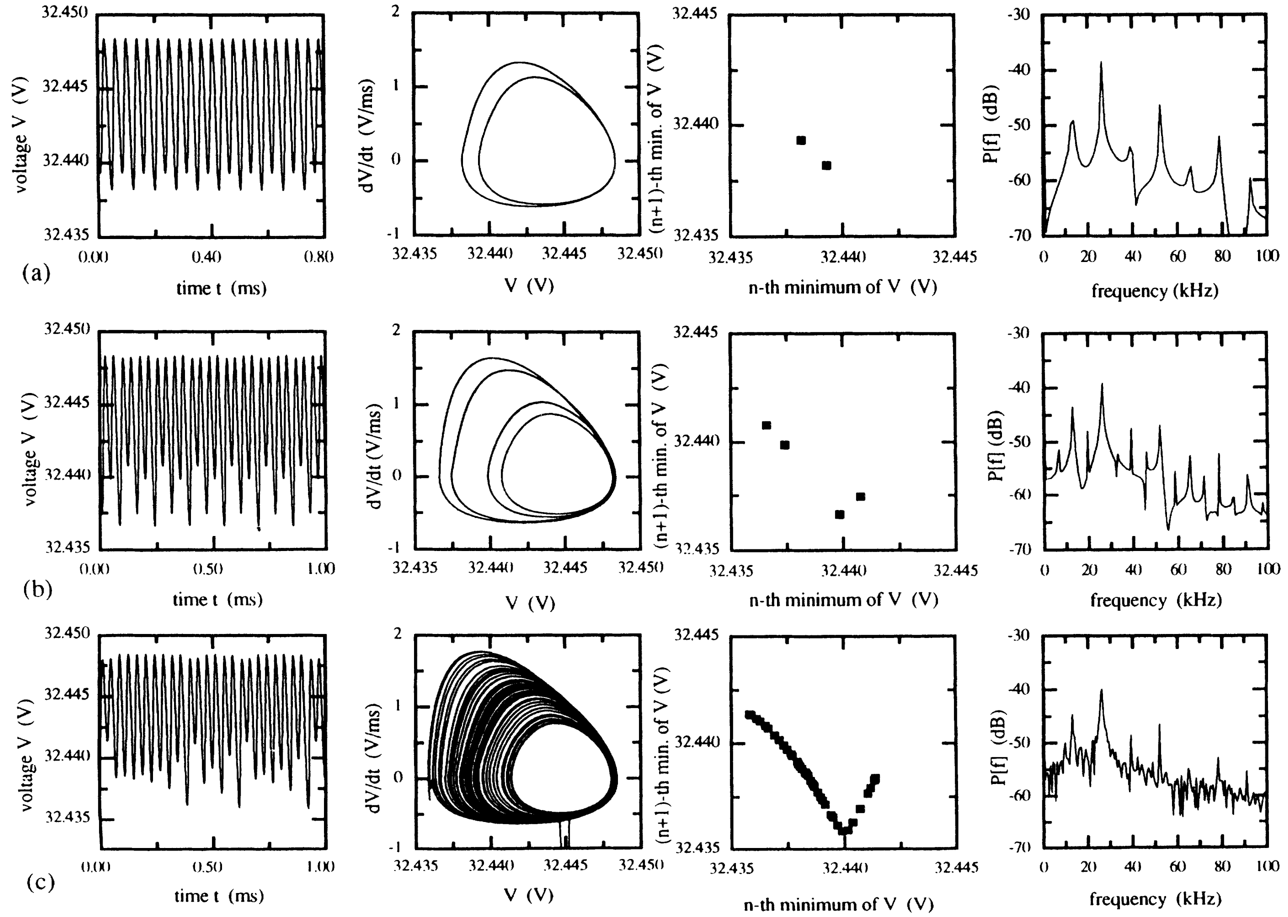

FIG. 8. Numerically calculated time trace $V(t)$, projection of the phase space onto the $\partial V/\partial t$-V plane, return map, and power spectrum for different values of V_s; parameters as in Fig. 7.

periodic wall oscillations reveals no periodicity. There is still a strong correlation between the global signal and the local filament motion. As example we point out that each large elongation of the filament wall is connected with a local maximum in the current $I(t)$ and a corresponding local minimum in the voltage signal $V(t)$. In addition to the time traces, the projections of the phase space onto the $\partial V/\partial t$-V plane, the return maps, obtained by plotting the $(n+1)$th vs the nth minimum of $V(t)$, and the power spectra of the three time series are shown in Fig. 8. For the nonperiodic time trace $V(t)$, the power spectrum is quite broad and relatively smooth in comparison with those of the periodic signals. Furthermore, the form of the phase-space projection and the return map indicate chaotic behavior of $V(t)$. An evaluation of five nonperiodic time series that contain data with a digitizing resolution of 8 bits supplies attractor dimensions between 1.87 and 1.94, using the algorithm from Grassberger and Procacia[19] with a modification described in Ref. 20; so we have strong hints for a chaotic wall motion of the current filament in this case.

4. Transition to a traveling localized filament

The current interval in which nonperiodic oscillations can be stabilized is very small and contains only some hundreds of microamperes. As indicated already in the threshold diagrams, e.g., in Fig. 7(c), the filament is able to separate from the boundary. Indeed, a complete separation of the filament takes place if the total average current is large enough. As shown in Fig. 9(b), the filament oscillates for a certain period of time near one of the system boundaries. During this stage, the amplitude of the wall oscillations increases in course of time. If the amplitude exceeds a threshold value, the filament is detached from the boundary and travels with a constant velocity of about $v=60$ μm/μs through the sample. When it reaches the opposite boundary the filament is reattached there, oscillates another few periods near the boundary with increasing breathing amplitude, and, finally, travels back to the right boundary. This superposition of breathing and traveling motion becomes visible in the voltage trace $V(t)$ of Fig. 9(a), too: on the one side, the relatively small local minima in this trace are accompanied by maximum filament elongations during the breathing oscillation. The decrease of these minima in course of time between the points t_1 and t_2 marked in Fig. 9(a) corresponds to an increase of local maxima in the current trace $I(t)=[V_s-V(t)]/R_0$ and indicates the growing breathing mode. On the other side, the global minima of $V(t)$ [Fig. 9(a), between t_5 and t_6] coincide

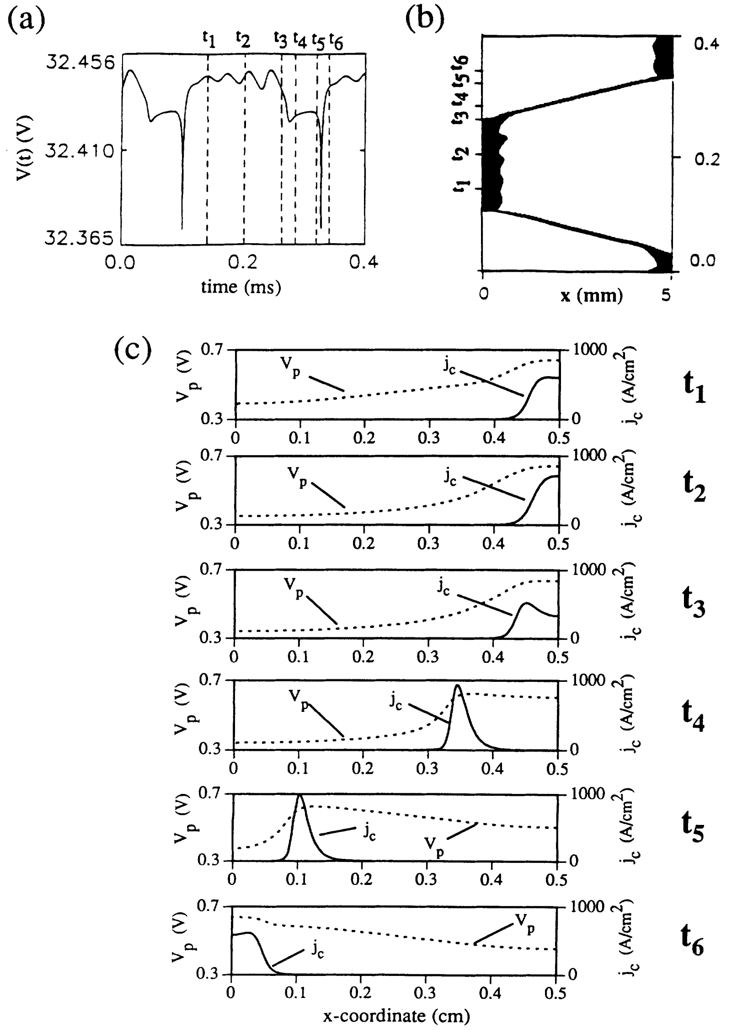

FIG. 9. (a) Numerically calculated time trace $V(t)$, (b) spatiotemporal evolution of $j_c(x,t)$, and (c) distributions $V_p(x)$ and $j_c(x)$ for different times during the travel from one boundary to the other; parameters as in Table I and $V_s=33.954$ V, $\bar{I}=1.512$ A, $t_1=140$ μs, $t_2=200$ μs, $t_3=260$ μs, $t_4=280$ μs, $t_5=320$ μs, $t_6=340$ μs with respect to the time zero in (a).

with those moments at which the traveling filament reaches one of the system boundaries. When the filament is traveling through the system, the device voltage and therefore the total current changes only little, revealing that the filament is moving with a constant shape.

In Fig. 9(c), the spatial distributions of $j_c(x)$ and $V_p(x)$ are drawn for the time steps t_1-t_6. On the basis of this representation, the mechanism leading to the transition from the boundary oscillation to the traveling filament and the inverse trapping process becomes plainly visible: the widely spread inhibitor V_p moves with a certain delay behind the activator j_c. This can be seen very clearly when the filament is in the traveling mode as in point t_4 of Fig. 9(c). The interplay of the so-called diffusion precursor[21] of the inhibitor distribution in front of the leading activator wall with the boundary of the system is essential for the reflection of the filament when it approaches the boundary. The Neumann boundary acts as a mirror for the filament and the inhibitor precursor of the imaginary filament interacts with the traveling filament, resulting in a reflection of the filament.[8] An immediate reflection of the filament, however, is prevented by the broad inhibitor tail that runs behind the activator distribution; the maximum of the inhibitor distribution and the inhibitor tail are still far away from the boundary when the activator maximum has already reached the boundary. As can be seen by looking upon the distributions $j_c(x)$ and $V_p(x)$ at the times t_1 and t_2, the inhibitor distribution concentrates near the activator distribution and decreases in the remainder of the sample during the oscillation near the boundary. This subsiding of the inhibitor far away from the activator maximum allows the renewed expansion of the activator to the interior of the system.

An increase of V_s, i.e., an increase of the average total current $\bar{I}$, leads to a more complex behavior of the oscillation near the sample boundary. With further increasing $\bar{I}$ the durations of breathing oscillations become smaller. Finally, when $\bar{I}$ exceeds 1.86 A the breathing oscillations near the boundary vanish completely and a well-defined traveling motion between the sample boundaries develops.

B. Calculations using mixed boundary conditions

The choice of Dirichlet boundary conditions for V_e is suggested by experimental results (cf. Sec. IV), which reveal that the current-density filaments do not develop directly at the boundary in general, but evolve in a certain distance, although rather close to the boundary. When we choose values for the emitter voltage $V_e(x=0,l_x)$ at the boundaries that are smaller than the value $V_{e,h}$ of the corresponding spatially homogeneous distribution determined by $q(V_e,V_i)=0$ and $Q(V_e,V_i,V)=0$, the filament is repelled from the boundaries as outlined in detail below. In experiment, a constant emitter voltage at the boundary may be motivated by surface effects. Especially for sufficiently large currents, there are some hints from measurements with a scanning electron microscope[22] that the effective feedback mechanism is weakened near the sample boundaries.

1. *Evolution of a static localized filament*

The formation of a localized current-density filament is very similar to the case with homogeneous Neumann boundary conditions. For boundary values of V_e larger than the value $V_{e,h}$ and for low total currents and sufficiently long samples, the current density decreases from the boundaries to the interior of the sample and $V_e(x)$ is nearly homogeneous far away from the boundaries. When the dc driving voltage is increased, in the environment of one of the boundaries a current-density filament is generated by contraction, as in the case with Neumann boundary conditions described in Sec. III A 1. This contraction is accompanied by the appearance of a negative differential resistance in the global current-voltage characteristic $I(V)$, as well. For a total current of 20 mA, the contraction phase is completed and the filament width reaches a minimum. In Fig. 10 stationary spatial distributions of j_c and V_p are drawn for a current at which the device is operating in the blocking mode and the conducting branch of the $I(V)$ characteristic, respectively. As can be seen clearly [Fig. 10(b)] the filament keeps away from the boundary having the value of $V_e(x=0,l_x)=0.63$ V. This is valid to less extent for the voltage distribution $V_p(x)$, which has its maximum value also well away from the boundary, but is not separated completely due to the relatively large spreading of V_p that represents the laterally extended inhibitor. The localization of the current filament in a well-defined distance from the boundary is a result of an interaction of the boundary with the filament. The interaction is attractive if the filament removes itself too far from the boundary and repulsive in the opposite case. This becomes evident when a stable stationary filament is thrown from its equilibrium position: in this case the elongated filament moves back and performs a damped oscillation around

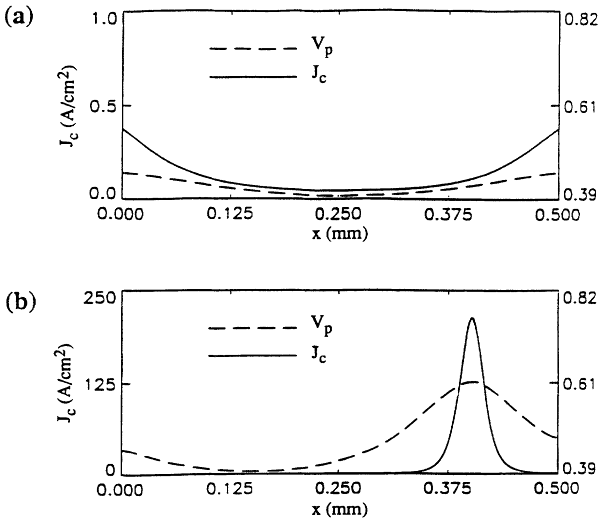

FIG. 10. Numerically calculated stationary spatial distributions of j_c and V_p for different values of the driving voltage V_s; parameters as in Table I and $V_e(x=0,l_x)=0.63$ V, $(V_s,I,R_0)=(65.57\text{ V},3.1\text{ mA},10\text{ k}\Omega)$ (a), $(32.85\text{ V},400\text{ mA},1\ \Omega)$ (b).

the stationary position, caused by the delayed response of the inhibitor with respect to the activator.

2. *Transition from a static to a rocking localized filament*

With increasing applied voltage V_s, i.e., increasing total current $\bar{I}$, the damping becomes smaller and at a critical current $I_{c1}=410$ mA a rocking motion of the current filament around the former equilibrium filament position appears [Fig. 11(a)]. Similar to the behavior in the case of homogeneous Neumann boundary conditions, the filament motion is accompanied by oscillations of the device voltage $V(t)$ [Fig. 11(b)]. A main qualitative difference in comparison to Neumann boundary conditions is the appearance of additional local extrema in the voltage signal. The maxima of $V(t)$, corresponding to minima in $I(t)$, appear when the filament turns back. In detail, the smaller local maxima belong to the inversion points situated in the interior of the sample, and the global ones are correlated with those moments at which the filament reaches the sample boundary. The voltage minima correspond to moments of maximal filament velocity. The two different kinds of minima are caused by the asymmetric filament reflection: when the filament is reflected from the boundary to the interior of the sample its velocity becomes larger than in the opposite case. The proper reason for this asymmetry is based on the influence of the Dirichlet boundary condition for V_e, which leads to a narrowing and a stretching of the current filament when it is reflected near the boundary or in the interior of the sample, respectively. We point out that there is no noticeable modulation of the amplitude of the current density when the filament is in the rocking mode.

For sufficiently small values of $V_e(x=0,l_x)$, i.e., smaller than the value $V_{e,h}$, the boundaries are exclusively repulsive. This leads to the formation of a symmetric current filament at the center of the sample and by exceeding the critical current to a symmetric rocking motion of the filament, because the reflection is governed by both boundaries in this case, being different from the case discussed here with $V_e(x=0,l_x) > V_{e,h}$.

As the applied voltage V_s is increased, and with it the total average current, the spatial amplitude l_r of the rocking filament as well as the peak-to-peak value of the global extrema of the voltage trace grow. In the following we denote the half of this peak-to-peak value as amplitude V_0 of the voltage trace. The scaling behavior of both quantities, l_r and V_0, is slightly different from that observed in the case of homogeneous Neumann boundary conditions. We find a square-root-like increase between l_r and $\bar{I}$, whereas V_0 increases linearly with $\bar{I}$. The difference between the scaling laws is not surprising, because the maximum filament elongations are correlated with the maxima in the voltage signal but not with the minima. The fundamental frequency f of the observed rocking oscillation rises at the bifurcation point discontinuously and decreases with increasing $\bar{I}$. From these results, the transition to the rocking filament can be classified as supercritical Hopf bifurcation; this is similar to the transition from a static to a breathing filament in the case of homogeneous Neumann boundary conditions.

3. *Transition from a rocking to a traveling localized filament*

The filament motion changes when the applied voltage V_s is so large that the rocking filament reaches the nearest sample boundary. In this case the spatial amplitude l_r reaches a value equal to the distance of the static filament from the boundary at a total current just below the critical current I_{c1}. The moving filament is then able to surmount the attractive influence of the boundary and travels through the whole sample. Reaching the other boundary the filament again is reflected at the boundary and turns back to the boundary it started from. This traveling between the boundaries repeats itself periodically. A typical filament motion of this kind is shown in the threshold diagram of Fig. 12(a). The global maxima in the corresponding voltage trace $V(t)$, Fig. 12(b), coincide in time with the reflection events at the boundaries. If the system is sufficiently long, the filament travels in a quasi-force-free region in the interior of the sample with an approximately constant velocity. We remark that the critical currents obtained for distinct boundary conditions are not identical.

The transition from the rocking to the traveling current filament is characterized by a sharp change in the fundamental frequency of the oscillation. The sharpness depends on the length of the sample. If we consider the motion for a current close to the bifurcation point, $\bar{I}=I_{c2}=605$ mA, but $\bar{I}>I_{c2}$, the filament can just surmount the virtual potential wall induced by the Dirichlet boundary condition for V_e and travels with a rather small velocity of about 30 μm/μs to the opposite boundary. Therefore, the fundamental frequency depends on the sample length and the sample current: the shorter the sample and the larger the current the larger the fundamental of the voltage oscillation.

As a result of the numerical calculations we can state

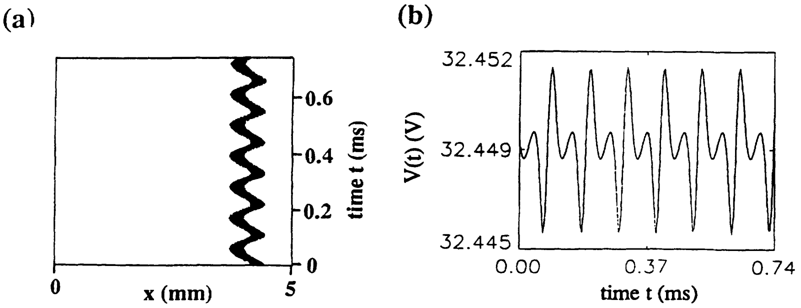

FIG. 11. (a) Numerically calculated spatiotemporal evolution of j_c and (b) time trace of the device voltage $V(t)$ in the case of a rocking current filament; parameters as in Table I and $V_s=32.9$ V, $\bar{I}=450$ mA, $V_e(x=0,l_x)=0.63$ V.

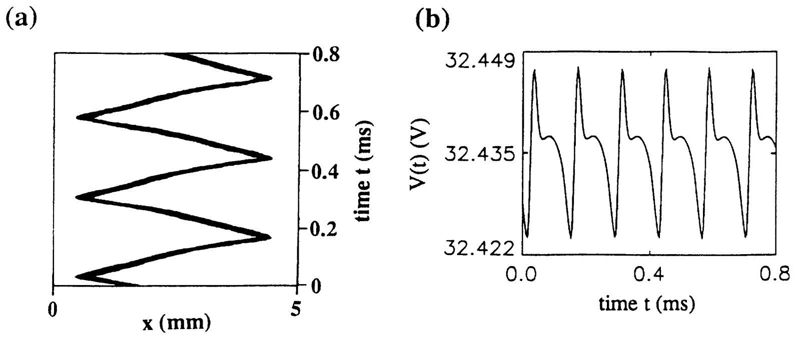

FIG. 12. (a) Numerically calculated time evolution of the spatial distribution of j_c and (b) time trace of the device voltage $V(t)$ in the case of a traveling current filament; parameters as in Table I and $V_s = 33.05$ V, $\bar{I} = 610$ mA, $V_e(x=0,l_x) = 0.63$ V.

that independent of the different boundary conditions, the fundamental solutions of the set of Eqs. (1), (3), and (6) can be classified as follows. For low total currents a homogeneous current-density distribution develops, at least far away from the sample boundaries. If the applied voltage V_s is sufficiently large, avalanche breakdown occurs and a static localized current filament appears, characterized by a typical width. This filament is stable in a certain interval of the total current. At a critical value I_{c1} a destablization of the static filament takes place and a spatial filament oscillation grows continuously as the total current increases, showing all the features of a Hopf bifurcation. At a second critical current I_{c2} a transition to a traveling filament occurs, characterized by a discontinuous jump in the fundamental frequency of the oscillation. This is a rough summing up of the bifurcation scenarios and their properties found in the system with homogeneous Neumann as well as mixed boundary conditions. The main differences between the solutions of Eqs. (1), (3), and (6) that appear if different boundary conditions are used concern the shape of the static filament that develops in the case of Neumann boundary conditions directly at the sample boundary and in the case of mixed boundary conditions at a well-defined distance from the boundary. Furthermore, the destablization of the static filament differs in both cases: it transforms into a breathing filament with a superimposed amplitude oscillation or a rocking filament, respectively. Finally, we remark that the critical currents I_{c1} and I_{c2} are shifted down to lower values for mixed boundary conditions in comparison to Neumann boundary conditions.

IV. COMPARISON WITH EXPERIMENTS

In order to compare the above-mentioned results with experiments we fall back upon experimental results published in Refs. 8 and 9 and additionally present some new ones.

A. Measuring techniques

We have applied two different measurement techniques to determine the current density and the potential distribution in the sample. For detection of the current density the recombination radiation of band-band transitions has been used. The electroluminescence signal is particularly large near the p-n junctions and the n^--n^+ contact. As the p-n junctions are situated rather close to the anode, the radiation is most effective near both electrical contacts. A streak camera with an S1 photocathode allows the detection of infrared radiation of wavelengths up to 1.2 μm in one space dimension and temporally resolved. The results presented below have been obtained by focusing a small stripe of the xy plane (Fig. 1) to the streak camera. The stripe is aligned parallel with the anode, has a width of about 100–150 μm and includes the p^+-n^+-p transistor. From evaluations of calibrating measurements it follows that the electroluminescence signal is a good measure for the current density.

The second experimental method is based on the scanning of a potential probe across the xy surface (Fig. 1) of the sample. Since the electrical behavior of the device changes drastically if the sample is mechanically damaged, e.g., by contacting the probe, the measurements have mainly been performed in the n^- region rather close to the p-n^- junction. In our model, the voltage drop along the n^- layer has been neglected for simplification; however, experiments reveal that this voltage drop is certainly not very large, but still exists. In literature, much work has been done concerning the interpretation of potential measurements with a potential probe. Mayer *et al.*[23] have shown for silicon p-i-n diodes that the measured potential V_{pr} can be correlated to the average of the quasi-Fermi levels, respectively weighted with the product of the carrier concentration and mobility. The conditions in the n^- layer of the p^+-n^+-p-n^- device are to some extent comparable to those in the p-i-n diode: in both cases we have a slightly doped or intrinsic region in which holes from the one side and electrons from the other side are injected. In a first approximation, we tentatively compare the measured potential with the potential V_p of our model. Naturally, we do not expect quantitative agreement; however, typical features of the distribution, e.g., the width, should be comparable. More details about both experimental methods applied here can be found in Ref. 9.

B. Experimental results and comparison with numerical calculations

1. Transition from a homogeneous current distribution to a static localized filament

A measured current-voltage characteristic $I(V)$ of a p^+-n^+-p-n^- diode is shown in Fig. 13(a). As discussed above, there is a low-current branch due to the blocking properties of the middle n^+-p junction that allows only a small leakage current and a current of thermally generated carriers separated by the electric field at this junction. The radiation, induced by recombination of holes and electrons, is so weak in this operating range that no signal distinguishable from the noise of the S1 photocathode can be detected with the streak camera. Potential measurements, however, show a homogeneous distribution indicating a homogeneous current flow. At the lower end of the range of negative differential resistance (referring to the current values), the recombination radiation as well as the potential distribution are still homogeneous, as shown in Fig. 13(b) for a total current $I=6$ mA. We remark that the light-density distribution at this current is noisy, but significantly different from the noise of the photocathode. Near the boundaries the potential distribution shows some deviation from the homogeneous state. This may be rated as a sign that mixed boundary conditions are suitable conditions for numerical calculations. Self-organized structures are not visible at this current value, either in the potential or in the radiation distribution. As the total current is increased, a contraction of the light-density and the potential distribution can be observed. The stationary distributions shown in diagram B of Fig. 13(b) have been taken at a total current $I=10$ mA, a value at which the negative resistance is approximately minimal. For a total current of about 30 mA the contraction phase is completed and a localized current-density filament has been formed [Fig. 13(b), diagram C] near the left sample boundary ($x=0$). Obviously, the light-density distribution indicates a current-density filament well away from the boundary. Note that the exposure time to the streak camera for point C is only 1/500 in comparison to points A and B in Fig. 13(a).

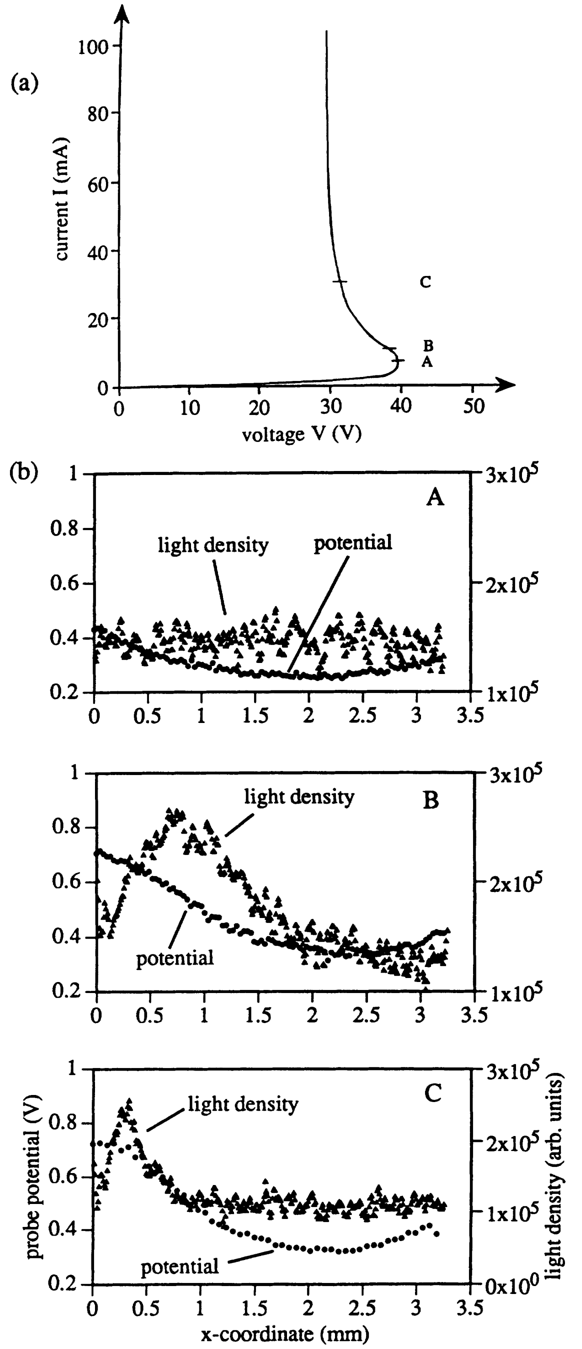

FIG. 13. (a) Experimentally determined current-voltage characteristic $I(V)$ of the p^+-n^+-p-n^- device and (b) stationary spatial distributions of the light density and the probe potential for different values of the driving voltage V_s corresponding to points A–C; parameters are $R_0=1.01$ kΩ, $T=318$ K, $(I,V_s)=(6$ mA,45.46 V) (A), (10 mA,48.86 V) (B), (30 mA,61.8 V) (C), exposure time for the streak image=250 s (A,B), 0.5 s (C).

In experiment, we find that the width of the current distribution is clearly smaller than that of the potential distribution, similar to the results of numerical calculations. The contraction procedure is completely reversible at any stage. The bifurcation from the homogeneous state to a filament takes place in a current interval between 5 and 30 mA in experiment and between 1 and 20 mA in the numerical calculations. A better agreement could be achieved by fitting the current saturation densities j_s, j_r, j_{SC}, and the leakage resistance ρ_L but is not done in the present work. Furthermore, in the calculations only one space coordinate is taken into account and the total current is obtained by assuming the same current density at any cross section in the z direction (Fig. 1). A cylindrical current-density filament with radially decreasing current density would be more realistic and would lead to a smaller total current.

An evaluation of the widths of the current-density and potential distributions shows that the experimentally observed contraction from the homogeneous state to a filament is reproduced by the model calculations in a satisfactory manner. As shown in Fig. 4, the widths decrease during contraction of the current and voltage distributions, reach a minimal value, and increase slightly for larger current values. We remark that the agreement between experimentally and numerically determined widths is even quantitatively good for large total currents.

2. *Transition from a static to a rocking localized filament*

When the average total current exceeds a critical value I_{c1}, the static localized current filament becomes unstable and a rocking filament motion develops. This rocking motion is correlated with oscillations of the voltage drop $V(t)$ across the device. In Fig. 14, a typical time trace $V(t)$ and a streak-camera record revealing the spatiotemporal evolution of the light-density distribution are shown. The bright regions correspond to regions of large light density. The correlation between the global voltage signal and the spatial filament motion differs from the results of numerical calculations. In experiment, we find that the extrema of the voltage signal correspond to the maximum elongations of the filament motion, at which the filament velocity becomes zero. In more detail, the voltage maximum coincides with the filament inversion point near the left sample boundary and the minimum with the turning back in the interior of the sample. In contrast to these experimental results, the minima in the numerically calculated global voltage trace in the case of mixed boundary conditions, whose application led to a rocking filament, appear in those moments in which the filament reaches its maximum velocity, as outlined in detail in Sec. III B 2.

We have investigated about twenty samples whose typical dimensions are shown in Fig. 1. The critical currents at which the destabilization of the static localized filaments takes place vary between 100 and 300 mA. The fundamental frequencies of the oscillations are typically in a range between 1 and 8 kHz. With the parameters of Table I, the numerical calculations lead to critical currents of about 400 mA and a rocking fundamental of about 10 kHz. A better agreement between experiment and the results of numerical calculations is achievable by fitting the emitter capacity C_e and the effective lifetime τ. However, in experiment, the rocking amplitude as well as the voltage amplitude start from zero at the bifurcation point and increase continuously with increasing total current, whereas the fundamental frequency is definitely larger than zero at the bifurcation point, indicating a supercritical Hopf bifurcation as in the numerical calculations. As already reported in Ref. 8, the amplitude l_r of the rocking motion shows a square-root dependence on the average total current $\bar{I}$, and the fundamental frequency decreases linearly with $\bar{I}$. This is consistent with the numerical results. For the increment $\Delta l_r^2/\Delta\bar{I}$ we obtain about 7000 μm^2/mA in experiment and about 1400 μm^2/mA in numerical calculations. These values are the results of linear fits to the measured and calculated $l_r^2(\bar{I})$ values. For the decrement $\Delta f/\Delta\bar{I}$ we obtain values between 18 and 34 Hz/mA as a result of experimental measurements and 15 Hz/mA from numerical calculations with the standard parameter set. The data for the increment $\Delta l_r^2/\Delta\bar{I}$ are based on measurements on a single sample; for the decrement $\Delta f/\Delta\bar{I}$ measurements on five different samples have been evaluated.

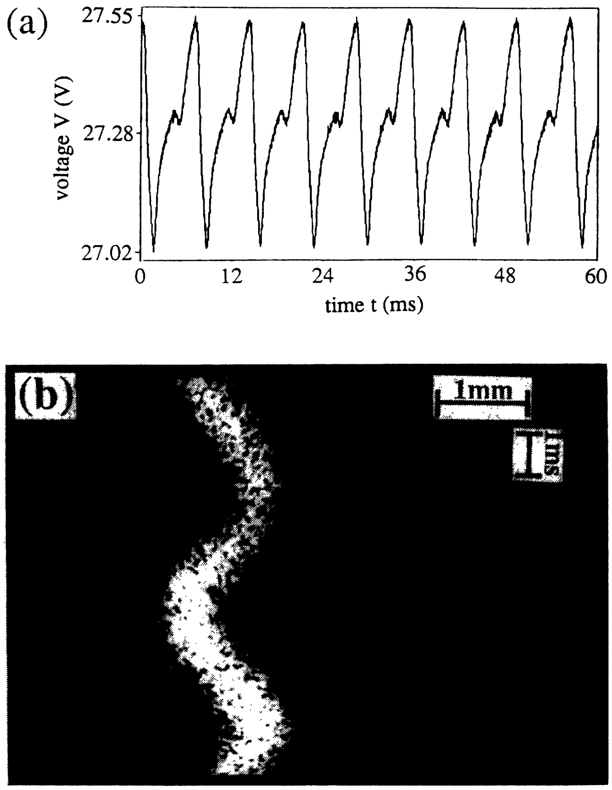

FIG. 14. (a) Experimental voltage trace and (b) streak-camera record of the light density in the case of a rocking current filament; parameters are $R_0=80$ Ω, $T=295$ K, $V_s=43.3$ V, $\bar{I}=200$ mA.

From the above-mentioned results, we can state that the experimentally observed bifurcation from a static to a rocking current filament is reproduced by numerical calculations with mixed boundary conditions qualitatively very well. Even the order of magnitude of the critical current, the fundamental frequency at the bifurcation point, the increment $\Delta l_r^2/\Delta\bar{I}$, and the decrement $\Delta f/\Delta\bar{I}$ agree in a satisfactory manner, although no sophisticated fitting procedure has been used. We remark that a comparison of potential measurements with numerically calculated potential distributions in the cases of dynamical structures is not possible at this stage, because the capacity of the potential probe used in conjunction with the necessarily high-Ohmic voltage measurements is too large for the detection of voltage signals in the kHz regime. Measurements with an active potential probe, which will eliminate this problem, are in preparation.

3. *Transition from a rocking to a traveling localized filament*

By a further increase of the total current in the experiment, a third transition occurs when a critical current I_{c2} is reached: the rocking motion is superimposed by a traveling motion of the filament. Near the bifurcation point, the superimposed filament motion presents itself as follows. The filament oscillates in the environment of one of the sample boundaries in the rocking mode. After a certain duration, which varies statistically, it travels to the other sample boundary, performs there some rocking oscillations, then turns back to the boundary it started from, and the process repeats itself. With increasing average total current the durations of the rocking oscillations become smaller and smaller, and finally a pure traveling motion of the filament between the sample boundaries takes place. In the voltage signal $V(t)$ the superposition of rocking and traveling motions becomes visible usually as a superposition of small-amplitude oscillations correlated with the rocking motion and large-amplitude oscillations which are due to the traveling component.

In Fig. 15, the experimental result for a typical time trace $V(t)$ and the appertaining streak-camera record showing the spatiotemporal evolution of the light-density distribution are depicted. As in the case of rocking filaments, there is a strong correlation between the integral voltage signal and the traveling filament motion. The minima and maxima of the voltage signal correspond to moments where the filament is near the left and the right sample boundary, respectively. The filament velocity v is approximately constant during travel from one side to the other. Typical values observed experimentally lie in the range between 1 and 8 μm/μs and are smaller than those obtained from numerical calculations with mixed boundary conditions ($v = 30$ μm/μs). But as in the case of rocking filaments, a better agreement between experiment and calculations should be achievable by fitting the model parameters, in particular C_e and τ.

We remark that the interval of the average current in which rocking oscillations are stable and no traveling motion exists varies in the investigated samples from about 10 to 50 mA, whereas numerical calculations yield a pure rocking filament motion in a current interval of about 180 mA. This mismatch can be eliminated by choosing larger boundary values $V_e(x = 0, l_x)$, which lead to a smaller distance of the filament from the sample boundary. Finally, we point out that we have observed also experimentally a period-doubling cascade of a rocking filament into a chaotic rocking filament as described in detail in Ref. 24. This behavior is similar to the behavior of the breathing filament described in Sec. III A 3. There, in the case of homogeneous Neumann boundary conditions, the transition from a breathing to a traveling current filament was characterized by a period-doubling sequence, which results in an irregular behavior of the filament wall when the total current is increased. Using the standard parameter set with mixed boundary conditions, which lead to a rocking instead of to a breathing filament, we did not find such a period-doubling sequence in the transition region between a rocking and a traveling filament; but it is not excluded that it is possible to find such a behavior for slightly modified parameters.

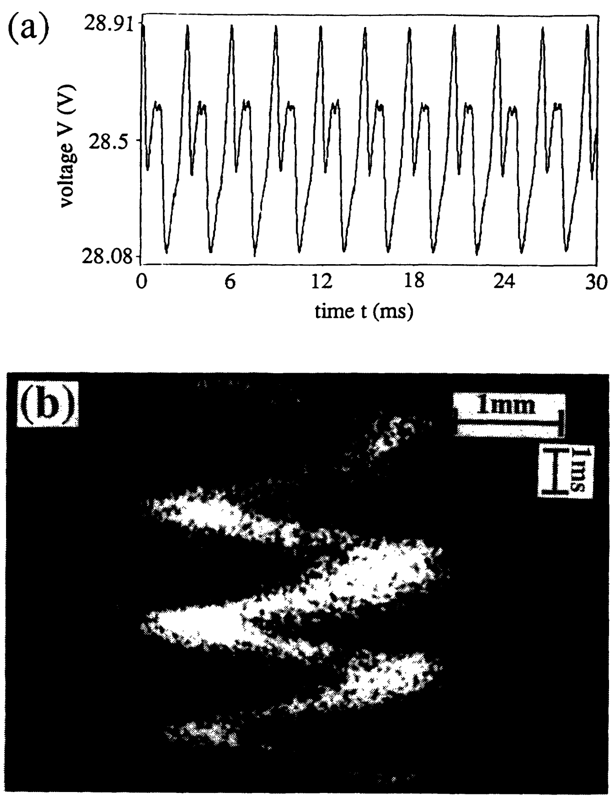

FIG. 15. (a) Experimental voltage trace $V(t)$ and (b) streak-camera record of the light density in the case of a traveling current filament; parameters are $R_0 = 163$ Ω, $T = 295$ K, $V_s = 95.3$ V, $\bar{I} = 410$ mA.

V. CONCLUSIONS

In the present work the spatiotemporal behavior of localized current-density filaments in p^+-n^+-p-n^- devices has been discussed. We have presented results of numerical calculations of a simplified two-layer model for different boundary conditions. For low total currents the device forms a homogeneous current-density distribution for homogeneous Neumann boundary conditions as well as for mixed boundary conditions. In the latter case only some deviations near the sample boundaries occur. In both cases a stable localized current filament develops for larger currents and spatiotemporal instabilities occur at a critical current I_{c1}. A detailed numerical analysis reveals that the stable filament becomes unstable with respect to oscillations of the width and the amplitude in the case of Neumann boundary conditions, whereas a rocking current filament develops in the case of mixed boundary conditions. The oscillations are a result of the delayed reaction of the inhibitor with respect to the activator and the interaction of the filament with the sample boundary. A suppression of the oscillation is possible if the ratio of the relaxation-time constants of the inhibitor and activator is reduced, e.g., by increasing C_e. We point out that the spatiotemporal oscillations are strongly correlated to oscillations of the global voltage drop $V(t)$ across the device and the total current $I(t)$. When a second critical current is reached, the breathing (Neumann boundary conditions) or rocking filament (mixed boundary conditions) transforms to a traveling filament that moves between the sample boundaries. We remark that the application of inhomogeneous Neumann boundary conditions leads to similar results as in the case of homogeneous Neumann boundary or mixed boundary conditions for sufficiently small or large values of the gradients, respectively.

In experiment, a bifurcation sequence from a homogeneous current distribution to a localized static current filament, followed by a transition to a rocking, and, finally, to a traveling current filament, has been observed in p^+-n^+-p-n^- diodes. All in all, this sequence is reproduced best by the numerical calculations with mixed boundary conditions. Within experimental error, satisfactory agreement between experimental and numerical results could be achieved concerning the filament width, the fundamental frequency of rocking filaments, and the dependence of the fundamental and the spatial amplitude of the rocking oscillation on the total current. Beyond that, the critical currents at which bifurcations set in could be approximated much better if appropriate parameters are fitted to experiment.

ACKNOWLEDGMENTS

The authors benefited from fruitful discussions with B. S. Kerner and would like to thank M. Möller for calculating the attractor dimensions and S. Kottemer for his technical assistance. Furthermore, a grant from the Deutsche Forschungsge-meinschaft is acknowledged.

---

[1] K. Aoki and K. Yamamato, Phys. Lett. **98A**, 72 (1983).

[2] B. S. Kerner and V. F. Sinkevich, Pis'ma Zh. Eksp. Teor. Fiz. **36**, 359 (1982) [JETP Lett. **36**, 436 (1982)].

[3] K. M. Mayer, J. Parisi, and R. P. Huebener, Z. Phys. B **71**, 171 (1988).

[4] A. Brandl, M. Völcker, and W. Prettl, Solid State Commun. **72**, 847 (1989).

[5] K. M. Mayer, R. Gross, J. Parisi, J. Peinke, and R. P. Huebener, Solid State Commun. **63**, 55 (1987).

[6] B. S. Kerner, B. P. Litvin, and V. I. Sankin, Pis'ma Zh. Tekh. Fiz. **13**, 819 (1987) [Sov. Tech. Phys. Lett. **13**, 342 (1987)].

[7] D. Jäger, H. Baumann, and R. Symanczyk, Phys. Lett. A **117**, 141 (1986).

[8] F.-J. Niedernostheide, B. S. Kerner, and H.-G. Purwins, Phys. Rev. B **46**, 7559 (1992).

[9] F.-J. Niedernostheide, M. Arps, R. Dohmen, H. Willebrand, and H.-G. Purwins, Phys. Status Solidi B **172**, 249 (1992).

[10] F.-J. Niedernostheide, R. Dohmen, H. Willebrand, H.-J. Schulze, and H.-G. Purwins, in *Nonlinearity with Disorder,* edited by F. Abdullaev, A. R. Bishop, and S. Pnevmatikos, Springer Proceedings of Physics Vol. 67 (Springer-Verlag, Berlin/Heidelberg, 1992), pp. 282–309.

[11] V. V. Gafiichuk, B. I. Datsko, B. S. Kerner, and V. V. Osipov, Fiz. Tekh. Poluprovodn. **24**, 1282 (1990) [Sov. Phys. Semicond. **24**, 806 (1990)].

[12] A. Wacker and E. Schöll, Semicond. Sci. Technol. **7**, 1456 (1992).

[13] E. Schöll and D. Drasdo, Z. Phys. B **81**, 183 (1990).

[14] G. Hüpper, K. Pyragas, and E. Schöll, Phys. Rev. B **47**, 15 515 (1993).

[15] U. Middya, M. D. Graham, D. Luss, and M. Sheintuch, J. Chem. Phys. **98**, 2823 (1993).

[16] U. Middya, M. Sheintuch, M. D. Graham, and D. Luss, Physica D **63**, 393 (1993).

[17] F.-J. Niedernostheide, R. Dohmen, H. Willebrand, B. S. Kerner, and H.-G. Purwins, Physica D **69**, 425 (1993).

[18] A. Gierer and H. Meinhardt, Kybernetik **12**, 30 (1972).

[19] P. Grassberger and I. Procaccia, Phys. Rev. A **28**, 2591 (1983).

[20] M. Möller, W. Lange, F. Mitschke, N. B. Abraham, and U. Hübner, Phys. Lett. A **138**, 176 (1989).

[21] B. S. Kerner and V. V. Osipov, Usp. Fiz. Nauk **157**, 201 (1989) [Sov. Phys. Usp. **32**, 101 (1989)].

[22] A. Wierschem, F.-J. Niedernostheide, A. Gorbatyuk, and H.-G. Purwins (unpublished).

[23] J. W. Mayer, O. J. Marsh, R. Baron, R. Kikuchi, and J. M. Richardson, Phys. Rev. **137**, 295 (1965).

[24] F.-J. Niedernostheide, M. Kreimer, H.-J. Schulze, and H.-G. Purwins, Phys. Lett. A **180**, 113 (1993).

[25] S. M. Sze, *Physics of Semiconductor Devices,* 2nd ed. (Wiley, New York, 1981).

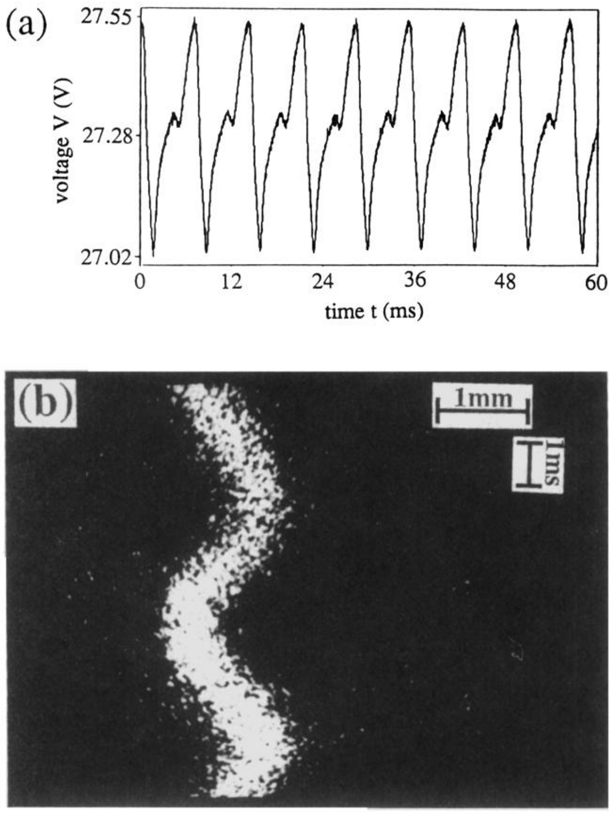

FIG. 14. (a) Experimental voltage trace and (b) streak-camera record of the light density in the case of a rocking current filament; parameters are $R_0=80\ \Omega$, $T=295$ K, $V_s=43.3$ V, $\bar{I}=200$ mA.

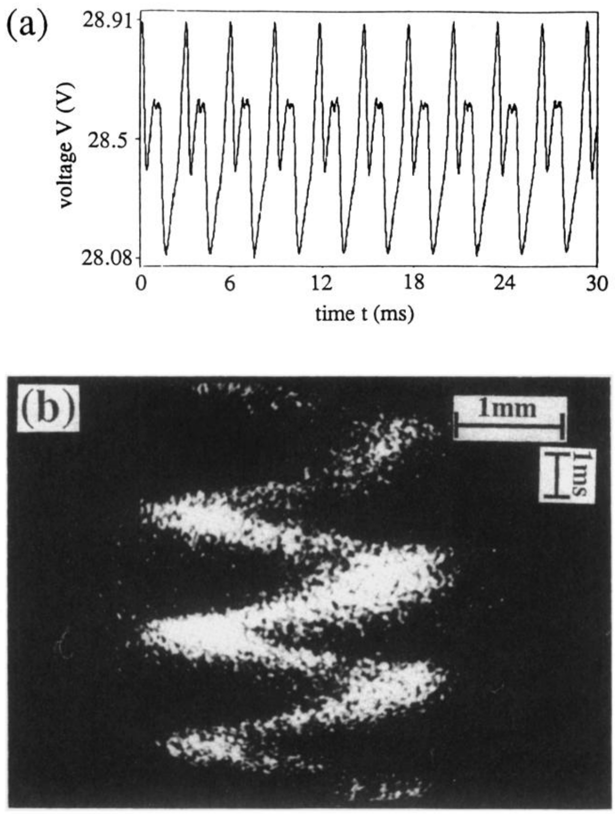

FIG. 15. (a) Experimental voltage trace $V(t)$ and (b) streak-camera record of the light density in the case of a traveling current filament; parameters are $R_0 = 163\ \Omega$, $T = 295$ K, $V_s = 95.3$ V, $\bar{I} = 410$ mA.